CrossMark
click for updates

Effect of ferrous iron on the nucleation and growth of CaCO₃ in slightly basic aqueous solutions†

Fulvio Di Lorenzo,*[a] Alejandro Burgos-Cara,[bc] Encarnación Ruiz-Agudo,[b] Christine V. Putnis[cd] and Manuel Prieto[a]

The precipitation of calcium carbonate, $CaCO_3$ and the growth of calcite has been studied in aqueous solutions containing ferrous iron (Fe^{2+}). Two different types of bulk experiments have been carried out: nucleation experiments at constant pH, following the procedure developed by Gebauer *et al.* (2008), revealed the stabilisation of aragonite induced by the presence of the foreign ions at the expense of calcite and vaterite. Growth experiments, using the constant composition method (Tomson and Nancollas, 1978), clearly showed that calcite growth is inhibited by the presence of Fe^{2+} and the characterisation of the regrown calcite crystals by HR-TEM confirmed the predictions obtained with molecular dynamics simulations. Additionally, *in situ* atomic force microscopy (AFM) flow-through growth experiments directly showed the distortion of the normal calcite growth spirals that lead to macroscopic inhibition of calcite growth. Finally, thermodynamic considerations for the solid solution – aqueous solution system Ca–Fe–CO_2–H_2O are discussed that allow the modelling of geochemical processes involved in this system, such as geological carbon storage in basaltic rocks.

Introduction

As a result of the drastic increase in atmospheric CO_2 recorded in the last few decades, due to anthropogenic emissions (Intergovernmental Panel on Climate Changes: Assessment Reports since 1990), current and future research is aimed at understanding and attempting to mediate this increase. Geological carbon storage (GCS) is a promising technology, that scientific research is focused on, as a potential means to remediate the increasing levels of atmospheric CO_2.[1] Many carbon capture and storage (CCS) initiatives all around the world are assessing the feasibility of different technologies to obtain sustainable, permanent and safe CO_2 storage.[1,2] An overview of the different technologies available for CCS was published by Elements[3] in 2008 and by Reviews in Mineralogy and Geochemistry[4] in 2013. Moreover details on the geochemical processes can be found in Geological Sequestration of Carbon Dioxide by Luigi Marini.[5] After pioneering projects based on the injection of supercritical CO_2 into empty fossil fuel reservoirs, interest has been focused on the concept of *in situ* mineralisation achieved by injecting CO_2 dissolved in water into basaltic rocks.[6,7] In this context, a thorough knowledge of the geochemical processes involving the formation and stability of carbonate phases is essential, especially for calcium and iron, two of the main divalent cations potentially available for CO_2 mineralisation in basaltic formations.[8]

The effects produced by numerous divalent cations on the growth of $CaCO_3$ have attracted a significant amount of research for decades, and in the last few years renewed interest has been focused on this system due to the new insights into the nucleation pathways of calcite and its polymorphs, provided by recent studies.[9–12] Anhydrous $CaCO_3$ has three different polymorphs (vaterite, aragonite and calcite, where the thermodynamic stability increases in the series), they have different stabilities and the most soluble is vaterite. Vaterite has been demonstrated to be a common intermediate during calcite formation from aqueous solutions.[13] The presence of foreign ions often stabilises vaterite and delays its conversion into calcite.[14] The life-time of vaterite crystals in contact with water is short due to its easy conversion into a more stable polymorph. On the contrary the transformation of aragonite into calcite is a slow process that is mainly a function of temperature, and it has been demonstrated that at temperatures lower than 50 °C this transformation is strongly hindered.[15] The system Ca–Fe–CO_2–H_2O has been widely studied during the last 50 years. Rosenberg[16,17] and Goldsmith *et al.*[18]

[a] *Department of Geology, University of Oviedo, 33005, Spain.*
 E-mail: fulvio@geol.uniovi.es
[b] *Department of Mineralogy and Petrology, University of Granada, 18071, Spain*
[c] *Institut für Mineralogie, University of Münster, 48149, Germany*
[d] *The Institute of Geoscience Research (TIGeR), Curtin University, Perth, Australia*

described the thermodynamic properties of the solid solution between the end members calcite ($CaCO_3$) and siderite ($FeCO_3$) using both synthetic and natural samples. To our knowledge, there are no reports of natural occurrences of pure ordered ankerite ($CaFe(CO_3)_2$), while disordered (Ca,Fe) CO_3 has been synthesized at 845 °C and 3 gPa.[19] Despite the rarity of this system, the occurrence of ferroan-dolomite in structured $Ca(Fe,Mg)(CO_3)_2$ solid solutions is quite common, where iron partially substitutes Mg according to the formula $(Ca(Fe_xMg_{1-x})(CO_3)_2, 0 \leq x \leq 0.7)$, demonstrating that partial substitution between iron and magnesium plays a fundamental role in determining stability of these phases.[8] Ankerite $CaFe(CO_3)_2$ and dolomite $CaMg(CO_3)_2$ stability was determined using calorimetric methods by Chai and Navrotsky,[19] and their study revealed that increasing the substitution of Fe for Mg produces opposite effects on the stability of ordered and disordered phases: the enthalpy of formation of disordered (Ca,Fe)CO_3 is more exothermic with an increase in the Fe content (and hence more stable), while for Fe-rich ordered ankerite it is less exothermic. The enthalpy of disordering for ordered ankerite is known to be significantly smaller (~10 kJ mol^{-1}) than that of ordered dolomite (~25 kJ mol^{-1}), which confirms the difficulty of obtaining pure ordered $Ca,Fe(CO_3)_2$ in contrast with the common occurrence of ordered dolomite.[19]

The aqueous solution becomes supersaturated with respect to siderite at lower concentrations than with respect to calcite as a result of its lower solubility at 25 °C (p$K_{sp,sid}$ = 10.49 and p$K_{sp,cal}$ = 8.30)[8] but precipitation is hindered for kinetic reasons as proven by studies that investigated numerous different synthetic pathways.[20] Despite that, ferrous iron in solution initiates the formation of secondary phases such as oxy-, hydroxyl-iron nanoparticles (containing Fe^{3+}). These phases are difficult to identify because of their short lifetime due to degradation by atmospheric oxygen and the formation of numerous phases where iron initially presents both oxidation states. Attempts have been made using TEM by the EELS (electron energy loss spectroscopy) technique to assess the oxidation state of iron in the Fe-bearing secondary phases but exposure to atmospheric conditions and an electron beam, makes true identification almost impossible.[21]

In this context, our experiments aimed to elucidate the characteristics of the initial stages of formation of $CaCO_3$ in the presence of different amounts of Fe^{2+} in slightly basic aqueous solutions and the influence of Fe^{2+} on subsequent $CaCO_3$ polymorphic selection. Also, a second set of experiments was focused on the effect of Fe^{2+} on calcite growth at pH 8.5, using the constant composition method.[22,23] Previous studies[24] show the inhibitory effect of ferrous iron on calcite growth up to pH 7.5, although the authors used the free drift method.[25] As remarked by Zhang and Nancollas[26] the constant composition method used here, presents several advantages compared to the free drift method: (i) growth and dissolution can be determined more precisely, especially at low driving forces; (ii) the experiments can be carried out in small regions of the phase diagram avoiding side reactions;

(iii) large amounts of material can be grown on seeds to facilitate characterisation and (iv) the effect of additives on reaction rates can be monitored over longer periods while the driving force remains unchanged. Moreover, the constant composition method, as opposed to the free drift method, allows changes in reactivity, due to crystal surface properties, to be studied and the increase of the superficial area during growth is reflected in the attenuation of pH variation during a single experimental run.[26] Finally, thermodynamic considerations of the (Ca,Fe)CO_3 solid solution – aqueous solution system are presented, to provide a thermodynamic perspective, fundamental to describe geological processes associated with geological carbon storage.

Materials and methods

Materials

Analytical grade reactants ($CaCl_2$, $FeCl_2 \cdot 4H_2O$, Na_2CO_3, $NaHCO_3$, $CaCO_3$) from Panreac (purity > 99.9) were used to prepare standard solutions. Synthetic $CaCO_3$ seeds were homogenised to a maximum size Ø < 66 μm. The superficial area of the seeds was determined by N_2 adsorption (BET method, A = 0.0246 ± 0.0014 m^2 g^{-1}). Stock solutions were prepared using double filtered ultrapure water (resistivity = 18.2 MΩ). Samples were filtered through millipore filters Ø < 0.4 μm under vacuum and dried with absolute ethanol (Panreac). Liquid nitrogen was provided by Airliquide.

All the experiments with Fe^{2+} were performed using treated water (anoxic water) in order to avoid significant oxidation of Fe^{2+}. Ultrapure water was boiled for at least 30 min under a continuous flow of nitrogen, and then rapidly cooled with liquid nitrogen. In this way the oxygen content in the ultrapure water could be significantly reduced.[27] This anoxic water was immediately used to prepare the stock solutions and experiments began less than 15 minutes after the water temperature returned to 25 °C. During the nucleation and bulk-growth experiments (see below), gaseous nitrogen was gently bubbled a few millimetres under the liquid–gas boundary in the closed reactor in order to prevent the entry of air, thus delaying the oxidation of Fe^{2+}. According to Stumm and Lee,[28] at pH values above 8 the limiting step for Fe^{2+} oxidation is the supply and diffusion of oxygen.

Nucleation experiments

Nucleation experiments (ESI,† Fig. S1) were performed by adding a constant flux (8 μL s^{-1}) of a 10 mM $CaCl_2$ solution to a 100 mL mixture of sodium carbonate and sodium bicarbonate (20 mM) (Table 1), kept at 25 °C and stirred using magnetic stirrers. The pH was fixed at 9 during the whole experiment by the addition of NaOH (0.1 M) to compensate for the acidification induced by the precipitation of calcium carbonate (see reactions (1) and (2)). Different Ca_T/Fe_T ratios (10, 5, 2.5, 1.25 and 0.625) were used. The conductivity of the reaction media was continuously monitored using a conductivity probe (Metrohm), the concentration of free calcium [Ca^{2+}] was constantly measured through a specific ISE (ion

Table 1 Composition of solutions used in nucleation experiments

| Reactor (mmol K⁻¹)	Reactant 1 (mmol K⁻¹)	Reactant 2 NaOH (mmol K⁻¹)	$\left(\dfrac{Ca_T}{Fe_T}\right)_{in}$	$\left(\dfrac{Fe_T}{Ca_T}\right)_{in}$	$\left(\dfrac{\{Ca^{2+}\}}{\{Fe^{2+}\}}\right)_{ppt}$	$\left(\dfrac{\{Ca^{2+}\}+\{Fe^{2+}\}}{\{CO_3^{2-}\}}\right)_{ppt}$	$SI = \log\left(\dfrac{IAP}{K_{sp}}\right)_{ppt}$ Cal|Arg|Vtr	Phases (XRD)
C^{IV} 20	Ca_T 10, Fe_T 0	100	∞	0	∞	0.3251	1.66|1.51|1.09	Cal, Vtr
C^{IV} 20	Ca_T 10, Fe_T 1	100	10	0.1	63.86	0.4086	1.73|1.59|1.16	Cal, Vtr, FeO_x
C^{IV} 20	Ca_T 10, Fe_T 2	100	5	0.2	31.84	0.4255	1.73|1.59|1.17	Arg, FeO_x
C^{IV} 20	Ca_T 10, Fe_T 4	100	2.5	0.4	15.72	0.4786	1.75|1.61|1.19	Arg, FeO_x
C^{IV} 20	Ca_T 10, Fe_T 8	100	1.25	0.8	7.37	0.9044	1.89|1.75|1.33	Arg, FeO_x
C^{IV} 20	Ca_T 10, Fe_T 12	100	0.625	1.6	2.82	3.72	2.02|1.88|1.45	Arg, FeO_x

Ca = [CaCl₂]; C^{IV} = [NaHCO₃] + [Na₂CO₃]; Fe = [FeCl₂·4H₂O]; Cal = calcite; Vtr = vaterite; Arg = aragonite; FeO_x = iron oxy-hydroxyl nanoparticles. Ca_T and Fe_T are the initial total concentrations [mmol kg⁻¹]. $\{Ca^{2+}\}$, $\{Fe^{2+}\}$ and $\{CO_3^{2-}\}$ are the activities calculated with Phreeqc.[26] The subscript "in" refers to the initial solution while the subscript "ppt" refers to the solution composition at the moment when free $[Ca^{2+}]$ started decreasing.

selective electrode, Mettler Toledo) and transmittance was monitored with an optrode sensor for titration at a wavelength of 610 nm (Metrohm). Additionally the added volume of base and calcium chloride were constantly recorded.

Solid products were characterised by powder X-ray diffraction (XRD, Philips, PANalytical X'pert Pro), field-emission scanning electron microscopy (FESEM, Auriga FIB-FESEM), transmission electron microscopy and electron diffraction (TEM-SAED, FEI TITAN G2). The composition of the crystals was analysed by energy-dispersive X-ray spectroscopy (EDX) coupled to FESEM (Oxford instruments), electron energy loss spectroscopy in TEM (EELS), and electron micro-probe analysis (EMPA) (Cameca, SX100). The composition of solutions was determined by inductively coupled plasma mass spectrometry (ICP-MS, Thermo Scientific, Element II). Activity coefficients, supersaturation, speciation and other properties of the solutions were calculated with Phreeqc version 3.1.7. using the phreeqc.dat database.[29]

Growth experiments

Growth experiments (ESI,† Fig. S2) were carried out according to the constant composition method.[22,23,30] 100 mL of a supersaturated solution with respect to calcium carbonate (Ω = 6.46, SI = 0.81 with respect to calcite) was placed in a jacketed reactor with a magnetic stirrer and kept at 25 °C. The experiment started with the addition of 50 mg of synthetic calcite seeds initiating an immediate decrease in pH due to calcite growth according to reactions (1) and (2).

$$Ca^{2+} + CO_3^{2-} \leftrightarrow CaCO_3\downarrow \tag{1}$$

$$HCO_3^- \leftrightarrow CO_3^{2-} + H^+ \tag{2}$$
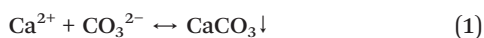
The pH was maintained constant at 8.5 by the addition of two titrants (ESI,† Table S1). Each titrant concentration was specifically calculated in order to raise the pH by a sodium carbonate/bicarbonate mixture (reactant 1, pH = 9) and in order to provide the right amount of $CaCl_2$ (reactant 2) to keep the supersaturation with respect to calcite constant. Both reactants were added automatically by the titration system from Metrohm (Titrando 905) and the software Tiamo (ver. 2.5, Metrohm). The curve described by pH value vs. time oscillated due to instrumental delay between pH recording and reactant addition as a response to pH threshold. Experiments ended when the superficial area of the growing crystals was too large (the superficial area is directly proportional to the growth rate, see eqn (5)) to allow pH to be kept constant, also increasing reactant addition to the maximum rate.

The calcite crystals were collected after the experiments, filtered and dried. Characterisation was done by powder X-ray diffraction using an aluminium holder. Crystals were also characterised by HRTEM and EMPA.

Additionally, the effect of aqueous Fe^{2+} on calcite spiral growth was directly observed by in situ atomic force microscopy (AFM, Bruker), using a fluid cell for a continuous solution flow.[31] Slightly supersaturated solutions (ESI,† Table S2) with different proportions of Ca_T/Fe_T, were injected over freshly cleaved $\{10\bar{1}4\}$ natural calcite surfaces[32] (Iceland spar, Chihuahua, Mexico).

Experiments were focused on the observation of calcite spiral growth, as this type of growth allows for accurate and individual measurements of the step advancement rate of non-equivalent steps formed on calcite cleavage surfaces.[33,34] To favour calcite spiral growth or hillock formation, solution compositions were optimized for a saturation index value of 0.77 and an activity ratio, $\{Ca^{2+}\}/\{CO_3^{2-}\}$, of 1.[31]

Results

Characterisation of iron precipitates

During the experiments, the system was supersaturated with respect to siderite and numerous iron oxides (e.g. hematite, wustite, goethite, lepidocrocite, magnetite, maghemite, calcium-ferrite and dicalcium-ferrite). Despite that, in our experiments we never observed precipitation of pure siderite, although other Fe-bearing phases were detected. Basic water solutions are highly oxidising in contact with air, but Fe^{2+} is

partially preserved by the formation of complexes and colloidal phases. The literature often refers to these phases as iron oxy-hydroxide flocculants due to their high variability in structure, short lifetime and rapid phase transitions, revealed by the changes in the colour of the precipitating solution seen with time.[35] This imposes technical limitations for the characterisation of Fe-bearing phases formed in the experiments. Complex formation[28] slows down the oxidation of Fe^{2+} and their formation was revealed by colour changes observed in the solution prior to any nucleation detectable by the other simultaneous measurements.

EELS analysis on the solid from a nucleation experiment (ESI,† Fig. S3, $Ca_T/Fe_T = 5$) revealed a 4:1 proportion of Fe^{2+}/Fe^{3+} in a hexagonal shaped secondary phase, after three days of ageing in the dry state at 25 °C. The hexagonal shape, Fe^{2+}/Fe^{3+} ratio and XRD reflections found for this precipitate, and for the other Fe-bearing experiments (ESI,† Fig. S4, sample from a nucleation experiment with $Ca_T/Fe_T = 2.5$), suggested that it is most likely green rust ($Fe^{II}_4Fe^{III}_2(OH)_{12}$-($CO_3$), PDF number #46-0098). The most intense reflections

of green rust ((003) and (006), d-spacing = 7.53 Å and 3.76 Å) were clearly observed in the diffraction pattern of the final solid product of the experiments.

For the nucleation experiments with high iron content ($Ca_T/Fe_T = 1.25$ and 0.625) the colour of the solution became intensely green during every experimental run. After filtration the solids changed from dark green to light brown (within the first hour) ending with a dark brown colour after some hours. Unfortunately, XRD diffraction with the PDF-2 database did not permit unambiguous identification of the low intensity reflections (ESI,† Fig. S4, Na_5FeO_4 is hypothesised). These most likely belong to the iron oxy-hydroxide nanoparticles that were observed by FESEM-EDX, EMPA and TEM. Their small average size did not allow their composition to be accurately determined, and electron diffraction showed a low-crystallinity.

The detection of green rust, some days after the experiments, with its high Fe^{2+} content demonstrated the effectiveness of the experimental setup to reduce Fe^{2+} oxidation and guaranteed that the effects attributed to Fe^{2+} and its aqueous
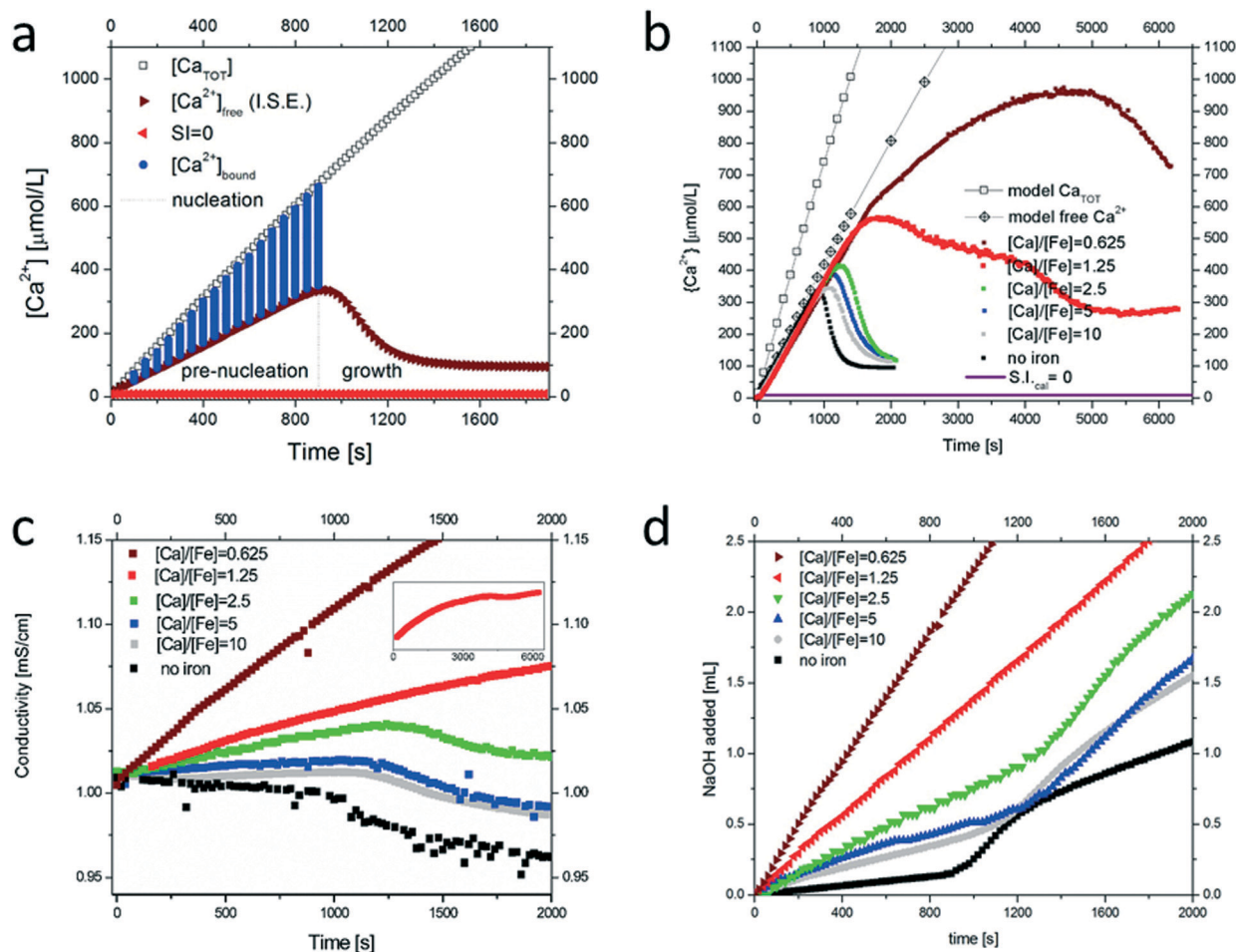

Fig. 1 a) Evolution of added calcium and measured free calcium showing evidence of ion pairing and/or clustering phenomena during the pre-nucleation regime. b) Influence of the amount of iron on the measured free calcium concentration during nucleation of $CaCO_3$. c) Evolution of the conductivity of the precipitating solution during nucleation experiments; the reduction seen at a certain point is consistent with a reduction in the total electrolyte concentration in solution related to $CaCO_3$ solid nucleation. d) The amount of NaOH added to keep the pH at 9 during nucleation experiments. A significant increase is seen with the increasing amount of Fe^{2+} in the reaction solution.

species would not be affected by significant amounts of Fe^{3+} due to the experimental setup and short experiment duration. Finally, previous work reporting calcite growth inhibition by iron at a lower pH (ref. 24) suggests that the effect of Fe^{3+} is similar to that seen here for Fe^{2+} but weaker, thus guaranteeing that the eventual oxidation could underestimate, but never overestimate, the observed inhibitory effect (see below).

Nucleation experiments

Nucleation experiments (Fig. 1) show a significant influence of ferrous iron on the pre-nucleation regime during calcium carbonate precipitation. Many other divalent cations such as Mg^{2+}, Ba^{2+}, Mn^{2+}, Sr^{2+}, Ni^{2+}, Co^{2+} etc. are well known to play a key role in controlling the reaction pathway and polymorphic relations in the system $Ca–H_2O–CO_2$.[36–40] Fig. 1a represents calcium measurements in an experimental run without Fe^{2+}. Before precipitation, the amount (mmol kg^{-1}) of total calcium added to the reactor, Ca_T, significantly differs from the free calcium $[Ca^{2+}]$ measured by the ISE probe. This is related to ion pairing and clustering phenomena in the pre-nucleation regime as stated by Gebauer et al.[9] When iron was added to the reaction vessel together with calcium, an analogous trend was observed. The fact that the slope of the linear part of the Ca-development curve in the pre-nucleation regime is not affected by the presence of ferrous iron suggests that iron does not have an influence on the formation of $[Ca^{2+}]–[CO_3^{2-}]$ pairs and/or pre-nucleation clusters. The nucleation experiments performed are characterised by a direct correlation between the elapsed time (proportional to added $[Ca^{2+}]$ because calcium is added at a fixed rate) and the actual supersaturation of the aqueous solution with respect to the different $CaCO_3$ polymorphs. The $[CO_3^{2-}]$ concentration remains approximately constant until nucleation occurred, because HCO_3^- is the most abundant carbon species in solution and the automatic NaOH addition to fix the pH at 9 implies that $[CO_3^{2-}]/[HCO_3^-] = k_{a2,carbonicacid}/pH = 4.5 \times 10^{-2}$ should remain more or less constant until pH varies. This means that the actual supersaturation with respect to the different $CaCO_3$ polymorphs could be estimated during the whole pre-nucleation step by simply looking at the actual free calcium recorded by ISE.

Nevertheless, the systematic addition of ferrous iron to this nucleation process (Fig. 1b) showed that the higher the Fe^{2+} concentration, the greater the measured free calcium concentration $[Ca^{2+}]$ at the onset of nucleation, implying higher supersaturation values with respect to $CaCO_3$ before nucleation occurred (Table 1). A similar effect could be also observed in the conductivity profiles (Fig. 1c) and in the added amount of NaOH (Fig. 1d). At the highest Fe^{2+} concentration tested, a particularly strong inhibition of $CaCO_3$ precipitation was found, evidenced by longer nucleation times and higher measured free calcium concentrations (~1 mM) at the onset of nucleation than in the control runs (i.e. no Fe^{2+} in the reaction medium).

The analysis by XRD of the main crystalline products formed in nucleation experiments confirmed that ferrous iron also influences $CaCO_3$ polymorph selection. For the control experiments (no iron) a mixture of calcite and vaterite was found, and analogously the experiments with $Ca_T/Fe_T = 10$ showed the same final products. When the Fe^{2+} concentration was increased ($Ca_T/Fe_T \leq 5$), aragonite became the most abundant phase (Table 1). FESEM observations (Fig. 2) confirmed that for the experiments with a $Ca_T/Fe_T = 10$ a mixture of vaterite and calcite was present in the precipitate. EDX and EMPA semi-quantitative analyses were performed on different crystals belonging to the same sample from a $Ca_T/Fe_T = 10$ experiment. The EDX results are only used to estimate the ratio Ca/Fe in the crystals (repeated measurements at different points, to minimize the distortion induced by the anisotropic structure of the crystal, showed an error about 10%) and not the unit formula established conforming to XRD phase identification. The amount of iron calculated for the calcite precipitates ($X_{Fe,cal} = 0.02$) was significantly lower than for vaterite ($X_{Fe,vtr} = 0.09$). The smallest Ca/Fe ratio was found in aragonite ($X_{Fe,arg} = 0.18$), but in this case a quantitative comparison was impossible because aragonite occurred only by doubling the maximum amount of iron allowed to precipitate calcite. It should be noticed that the doubling of the initial Fe^{2+} produced about one order of magnitude change in the mole fraction of the crystals confirming the greater ability of aragonite to host or incorporate iron in comparison with its rhombohedral polymorph, calcite.

Growth experiments

The experiments performed according to the constant composition method (ESI,† Table S1) revealed that the presence of iron in the growth solutions significantly slowed down the growth of calcite, delaying the onset of the pH drop at which the addition of the titration solutions could not maintain the pH of the system constant (Fig. 3). This clearly shows the inhibitory effect of iron on calcite growth.

Unfortunately, experiments with $Ca_T/Fe_T \leq 25$ followed a different trend because the inhibitory effect was too strong and calcite did not grow under these experimental conditions.

The AFM in situ growth experiments revealed a distortion of the normal rhombohedral spiral geometry due to the presence of iron (Fig. 4, also a multimedia file showing an experimental run is available).

The effect was particularly clear on the acute step where the straight steps, typically seen during pure calcite growth, were replaced by pinned steps according to the Cabrera and Vermilyea impurity incorporation model.[10,41] The shortening of the average step length, caused by Fe^{2+} adsorption at the step edges, slows the advancement of steps resulting in macroscopic inhibition of growth. Studies at the nanoscale on calcite growth and dissolution[11] demonstrated that step spreading rates are different for acute and obtuse steps, with the obtuse step spreading rate higher than the acute step
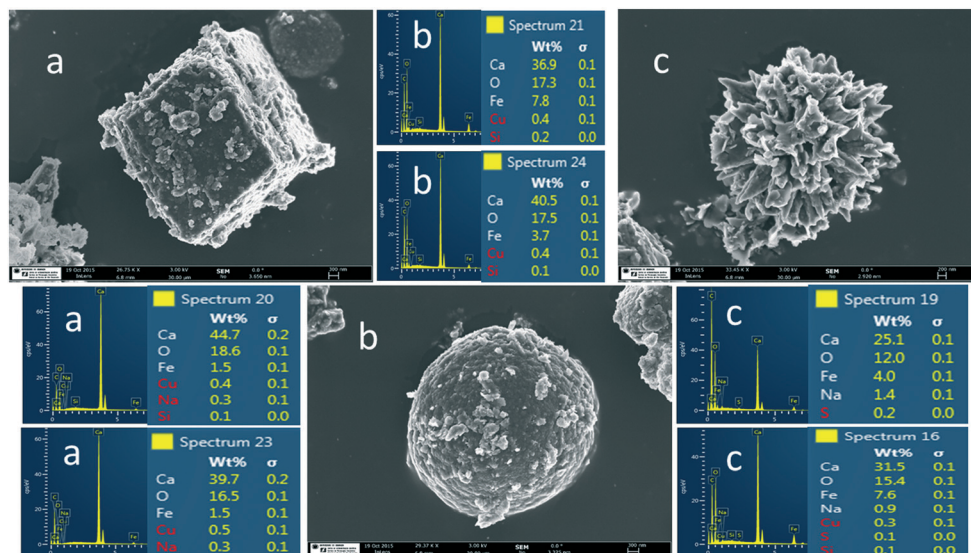
Fig. 2 FESEM secondary electron images and EDX analysis of the three polymorphs of CaCO₃ detected during the nucleation experiments. Calcite (a) and vaterite (b) came from the same experimental run of Ca_T/Fe_T = 10 while aragonite (c) came from a Ca_T/Fe_T = 5 experiment.
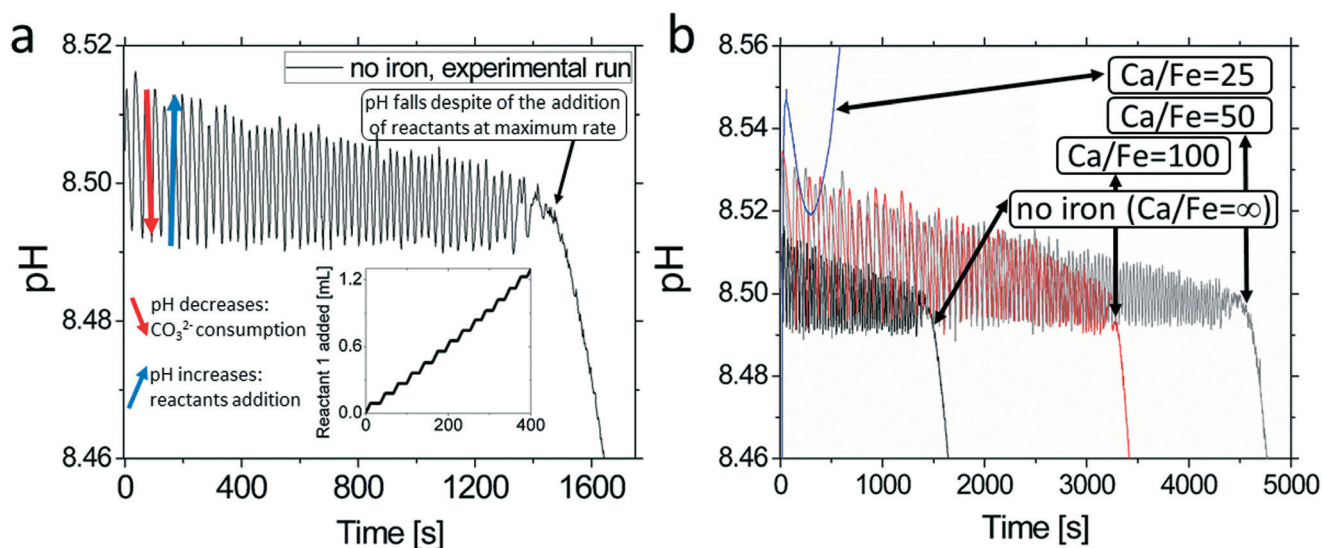

Fig. 3 a) pH *vs.* time plot recorded during an experimental run without iron. The inset represents the added volume of reactant 1 *vs.* time, the "stair" shape clearly marks the intermittent addition of the reactants during the initial cycles. b) The pH plots of experiments with different amounts of ferrous iron, showing the inhibitory effect on calcite growth induced by Fe²⁺. For Ca_T/Fe_T = 25 the growth inhibition was so pronounced that not even a single cycle was completed under these experimental conditions.

during both dissolution and growth.[42] We observed a geometrical distortion that occurs firstly on acute steps, while obtuse step geometry was not initially affected (Fig. 4). Less accessible sites continued growing, forming another spiral and confirming the key importance of experimental site selection (the lower left corner of Fig. 4).

Discussion

Nucleation experiments

In order to calculate the influence of ferrous iron on solution speciation in the Ca–H₂O–CO₂ system, we calculated the

moles of bound calcium ($n[Ca^{2+}]_{bound}$, Fig. 5a) as the difference between the moles of calcium added to the reactor (nCa_T) and the free calcium measured ($n[Ca^{2+}]$) using the ISE electrode.[9]

$$n[Ca^{2+}]_{bound} = nCa_T - n[Ca^{2+}] \tag{3}$$

By directly comparing experiments with and without Fe²⁺, the slope of the calcium bound *versus* time plot was not found to be influenced by Fe²⁺ in the pre-nucleation stage even for Ca_T/Fe_T < 1 (Fig. 1b). This excludes the possibility that any inhibitory effect of Fe²⁺ on CaCO₃ nucleation found in our
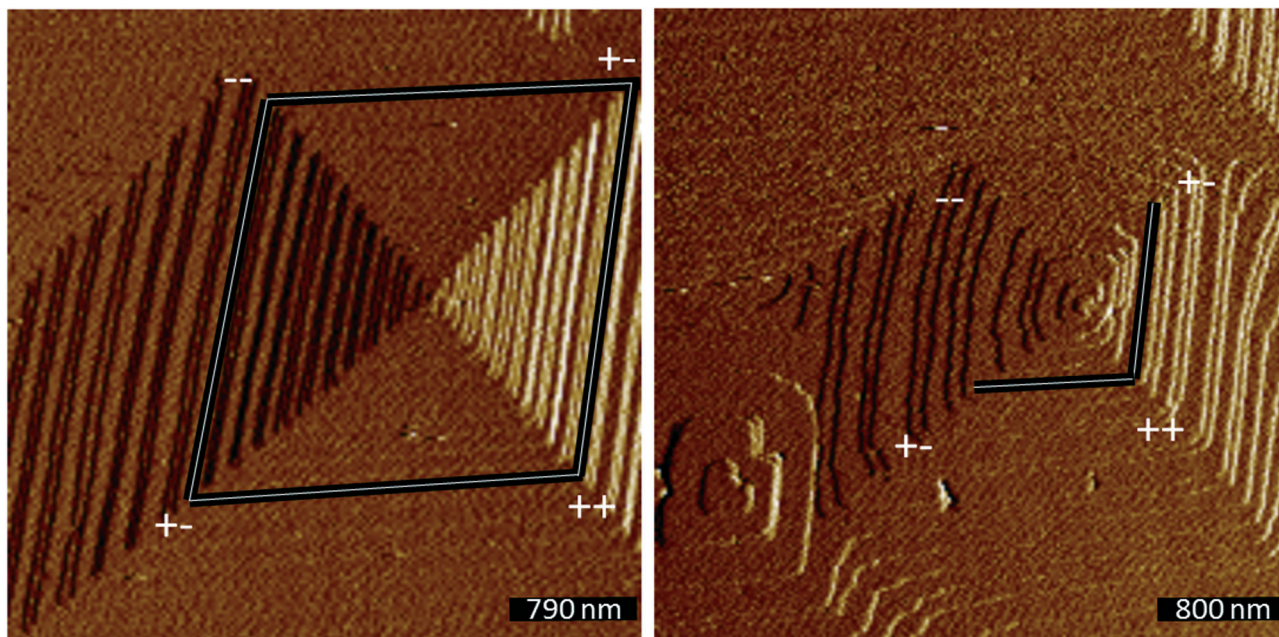
Fig. 4 AFM deflection images obtained working in contact mode, showing the geometrical distortion induced by the presence of Fe^{2+} on calcite growth spirals or hillocks. The left image shows the typical shape of a calcite hillock developed in pure (i.e. Fe-free) growth solution, grown by the interaction of a supersaturated aqueous solution with a {10$\bar{1}$4} calcite surface. Acute (—) and obtuse (++) steps are highlighted. The right image was recorded on the same hillock after 10 minutes of interaction with a supersaturated aqueous growth solution also containing ferrous iron (Ca_T/Fe_T = 12.5, ESI† Table S2).

experiments could be attributed to an alteration of the dynamics of the equilibrium of pre-nucleation species in solution.

Initially, the concentration of $[CO_3^{2-}]$ was the same in all experiments. As soon as free CO_3^{2-} is consumed by the interaction with calcium (forming ion pairs and/or clusters), the ratio $[CO_3^{2-}]/[HCO_3^-]$ changed and the pH decreased. The set up used in our experiments allowed online addition of NaOH that converted the excess of bicarbonate to re-equilibrate the carbonate to bicarbonate ratio in order to maintain the solution at pH = 9. The higher the Fe^{2+} in solution the higher the possible stabilization of pre-nucleation clusters containing both ions (Ca^{2+} and Fe^{2+}). Furthermore, the formation of ion pairs between Fe^{2+}/Fe^{3+} species and CO_3^{2-} may also result in the acidification of the system because of the equilibrium already explained (see also eqn (2)). This may explain the higher amounts of added NaOH necessary to maintain the pH constant.

For the control experiments without iron, the moles of carbonate bound ($n[CO_3^{2-}]_{bound}$) (Fig. 5b) due to the formation of ion-pairs and clusters between Ca^{2+} and CO_3^{2-}, can be calculated by equilibrium relations in the H_2O–CO_2 system and by the amount of base (Fig. 1d) used as titrant to keep the pH constant according to the equation:[9]

$$n[CO_3^{2-}]_{bound} = ([NaOH] \cdot V_{NaOH} \cdot 0.9572) \qquad (4)$$

where [NaOH] is the concentration of base [mol L^{-1}], V_{NaOH} is the volume of base added [L] and 0.9572 is a parameter function of pH and dissociation constants of carbonic acid.[9]

For a fixed time during the pre-nucleation step (600 seconds), it was possible to correlate the increase of NaOH necessary to achieve pH = 9 to the effects induced by different amounts of ferrous iron (Fig. 5c). The prerequisite step needed an offset of the values for $n[CO_3^{2-}]_{bound}$ in the post-nucleation stage, which should be matched with the values obtained for $n[Ca^{2+}]_{bound}$ (1 : 1 relationship) in the experiments without iron:[9] the assumption is that, in the post-nucleation region, all the added OH^- compensates for CO_3^{2-} consumption as $CaCO_3$ building units. The water chemistry of iron is significantly different to that of calcium due to its higher hydration energy, the formation of stable hydrated phases, its stronger Lewis acidity and the coexistence of different oxidation states. For all these reasons, an exact correlation between the excess of NaOH added and the formation of $[Fe^{2+}][CO_3^{2-}]$ is not possible. Our attempts clearly showed that the excess of NaOH added was considerably higher than the Fe_T present in the system (almost twice, Fig. 5c), confirming the impossibility to directly correlate the surplus of OH^-, added in presence of Fe^{2+}, with clustering phenomena between $[Fe^{2+}]$ and $[CO_3^{2-}]$ due to the significant presence of $[HCO_3^-]$, $[OH^-]$ and $[Cl^-]$. The formation of Fe^{2+} complexes and ionic pairs during the experiments with higher iron concentrations could be inferred by the observed colour changes of the solution during the pre-nucleation step. The colour transition (colourless to green) was observed prior to any variation in the monitored parameters (except for the visible light transmittance of the solution).

The increase in the amount of NaOH added, associated with the presence of Fe^{2+} in solution, could not be explained by the pH adjustment or by the formation of the Fe-bearing aqueous species included in Phreeqc (PHREEQC.DAT database). This software predicted the free $[Fe^{2+}]$ to be the major
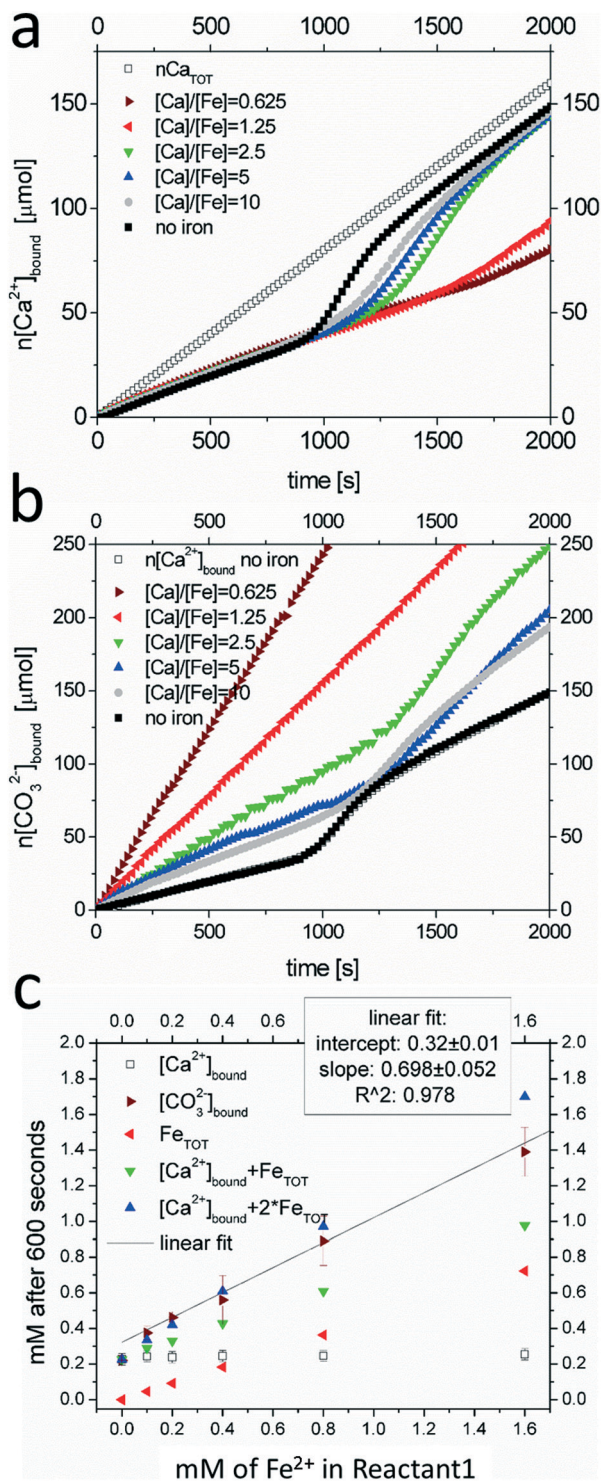
Fig. 5 a) Comparison between the moles of bound calcium during experiments with and without iron, the initial pre-nucleation segment is analogous in all experiments. b) The presence of iron induces a significant increase of NaOH required to maintain the pH at 9, proportional to its concentration. c) Bound species after 600 seconds (pre-nucleation part) showing the effect of the different Ca_T/Fe_T ratio studied: the amount of CO_3^{2-} bound is proportional to the Fe_{TOT} present in the system. The observation that this increment of CO_3^{2-} bound induced by Fe^{2+} is greater than the molarity of Fe_{TOT} suggests that possibly the association between Fe^{2+} and monovalent anions such as Cl^-, OH^- and HCO_3^- could play a role more important than predicted by models with Phreeqc (PHREEQC.DAT database).

species, or at least similar to the second most abundant $[Fe^{2+}][CO_3^{2-}]$. However our experiments (Fig. 5c), showed that the OH^- added doubles Fe_T, suggesting that the formation of $[Fe^{2+}][OH^-]_2$ could be more important than predicted by models. A lower availability of Fe^{2+}, due to $[Fe^{2+}][OH^-]_2$ species, could also contribute to the observation that the formation of siderite was never detected despite the higher supersaturation of the system compared to calcite (for example, after 600 seconds, for a $Ca_T/Fe_T = 10$, $\Omega_{calcite} = 30.9$ while $\Omega_{siderite} = 123$).

Growth experiments

The growth rate of calcite (R [mol s^{-1} m^{-2}]), normalized by the surface area of the seeds (A [m^2]), is often related to supersaturation (Ω) by the empirical equation:[43]

$$R = k \times A \times (\Omega - 1)^n \qquad (5)$$

where k and n are the rate constant and the rate order, respectively, fitting parameters. The volume of $CaCl_2$ added during the experiments was used to calculate the mass increment produced by crystal growth of calcite. The mass variation with respect to time, normalized with respect to the surface area (measured by N_2 adsorption and the BET equation), corresponded to the measured growth rate.

The first segment of the added volume of titrants (inset Fig. 3a) was fitted linearly to eqn (5) and the value of k was calculated under the assumption that the presence of iron does not affect the reaction order ($n = 2$). Rate changes during the whole experiment have been attributed by previous studies to the increase in surface area of the growing crystals.[31] The growth rate calculated in this way showed a significant decrease ($k_{noiron} = 2.(8) \times 10^{-07}$; $k_{CaT/FeT=100} = 6.(8) \times 10^{-08}$; $k_{CaT/FeT=50} = 8.(2) \times 10^{-08}$ [mol s^{-1}]) with small amounts of iron ($25 < Ca_T/Fe_T \leq 100$). For ratios ($Ca_T/Fe_T \leq 25$) it was impossible to determine a reliable value for the growth rate because the reaction resulted in a pH increase, unexpectedly according to previous considerations on calcite growth, possibly due to Fe-bearing secondary phase formation.

This inhibitory effect of ferrous ion was further studied *in situ* at the nanoscale within a fluid-cell of an AFM. These experiments revealed a strong distortion of the acute step during spiral calcite growth (Fig. 4). Previous work has investigated the effect of divalent cations on calcite growth by experimental, *in situ* techniques (especially Mg^{2+})[31,44] and by computational studies.[45] These studies have shown that the extent of impurity incorporation during calcite growth depends on the enthalpies of the reactions, the reduction of elastic strain and the relative strength of the water–cation interaction at the growing surface. By analogy with magnesium, the inhibition is significant due to the small atomic radius ($r_{Fe^{2+}} = 0.78$),[46] that easily allows the ion to be absorbed onto the small cavity (78°) of the acute step. Computational studies using molecular dynamic simulations[45,47] revealed that several impurities (Fe^{2+}, Mg^{2+}, Cd^{2+} and Sr^{2+}) are

preferentially incorporated at kink sites due to the favourable enthalpy and entropy of reaction.[48] The formation of an impurity-rich layer on the calcite surface induces a decrease of the thermodynamic driving force for growth (the process becomes endothermic) and, as a consequence, the growth rate decreases.

Our TEM characterisation of calcite crystals grown from Fe-bearing aqueous solutions (Fig. 6) experimentally demonstrates the results predicted by force-field simulations. Electron diffraction patterns allowed measurement of the d-spacing in the new layers re-grown in the presence of Fe^{2+}. Comparing the d-spacing for pure calcite and siderite (and assuming a linear variation of the d-spacing as a function of composition, "Vegard law"), it becomes evident that the incorporation of iron in the calcite structure induces a strong distortion of the lattice parameters. The theoretical amount of ferrous ion needed to induce a similar variation is extremely high ($Fe^{2+} > 35\%$); however, the Ca_T/Fe_T ratio in the growing solution was equal to 50 for this sample. This is a further confirmation of the reliability of molecular dynamics simulations in the system $Ca–Fe–CO_2–H_2O$.

According to the step pinning model[41] the absorption of strongly hydrated impurities on the step edges hinders step advancement, and the entry into the "dead zone" inhibits growth.[10,44] The incorporation of growing units into the crystal structure is a complex process composed of different steps;[42] each step is a reversible process characterised by an intrinsic activation energy. The first step needed to trigger the growth process is the absorption of cations onto the crystal surface.

From the point of view of the cation, this process implies the formation of a coordinate bond with the crystal surface,

the loss of freedom degree and the alteration of the hydration shell. Thereafter, the absorbed cation is still partially hydrated and the hydration shell continues losing H_2O molecules until its coordination is fully replaced by crystal units and the bonds evolve to equilibrium values for the specific crystal structure.

As soon as $CaCO_3$ units are substituted by $FeCO_3$, the resulting distorted lattice geometry does not allow Ca^{2+} to fit into the cation site. The geometrical constraint induced by iron incorporation makes calcite unable to grow normally (by addition of $CaCO_3$ building units) and the hydration of iron inhibits the propagation of growth by addition of $FeCO_3$ units. The combination of these two processes: lack of fitting of calcium ions and slow kinetics of dehydration of Fe^{2+} results in calcite growth inhibition *via* a surface passivation process. TEM measurements of our samples confirmed that the outer layers of calcite crystals host iron not only by absorption but incorporated into the crystal lattice as confirmed by the strong variation of d-spacing for reflections associated with the [110] and [116] crystallographic directions.

Ion partitioning in the system Ca–Fe–H₂O–CO₂

From a thermodynamic point of view, the distribution of iron between calcite and aqueous solution can be seen as an exchange reaction, such as:

$$CaCO_3 + Fe^{2+} \leftrightarrow FeCO_3 + Ca^{2+} \qquad (6)$$
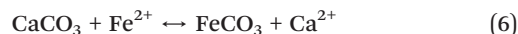
The solid solution $(Ca,Fe)CO_3$ is not complete and a number of works report a wide miscibility gap also at high temperatures ($T > 300\ °C$).[16–18,49] To our knowledge, no

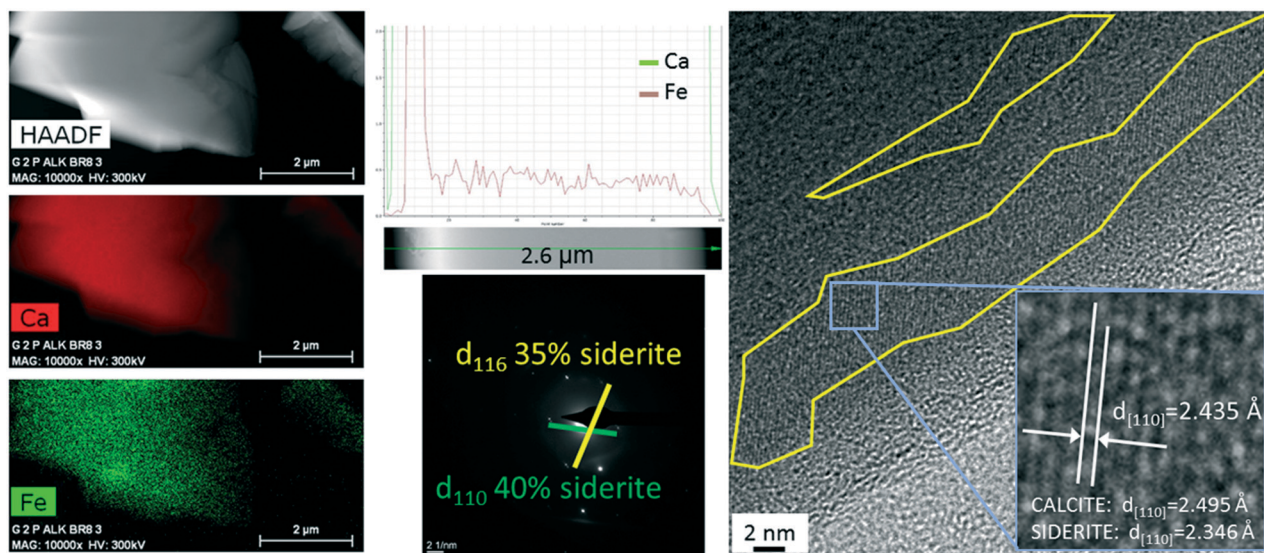**Fig. 6** Left column: HAADF compositional maps of calcium and iron, measured on a calcite crystal after a growth experiment ($Ca_T/Fe_T = 50$). Middle column: Top, the elemental composition profile demonstrating iron incorporation. Bottom: electronic diffraction pattern, which allows estimation of the lattice distortion produced by iron incorporation into the calcite structure. Right column: a high-resolution image emphasizing the existence of ordered domains and looking inside indicates the possibility to identify the observed surface as {110}: the observed d-spacing is significantly smaller than pure calcite confirming the incorporation of ferrous iron.

attempts have been made to describe at 25 °C the non-ideality of this system by calculating the sub-regular Guggenheim parameters[50,51] and to describe the thermodynamic ion partitioning. Previous works also support the derivation of mixing parameters from miscibility gap data with the lack of direct measurements.[51,52]

The miscibility gap values reported between 300–550 °C by Rosenberg[16] ($X_{FeCO_3}(1) = 0.04$; $X_{FeCO_3}(2) = 0.93$) show asymmetry with respect to the end members; each side of the miscibility gap has been fitted with an exponential function to extrapolate the gap limits at 25 °C ($X_{FeCO_3}(1) = 0.021$; $X_{FeCO_3}(2) = 0.931$). In order to obtain a more accurate approximation, values from Glynn[52] were also considered for the calcite-rich side, while for the siderite-rich side they were not considered due to the strong deviation with respect to Rosenberg and Goldsmith's values.[16–18] To describe the properties of this system we use a sub-regular solid solution model (dimensionless Guggenheim parameters: $a_i \neq 0$, $i = 0, 1$; $a_j = 0$, $j \geq 2$).[53–55] At the miscibility gap boundaries, the chemical potentials of each solid component (μ_{FeCO_3}, μ_{CaCO_3}) are expressed by eqn (7) and (8):

$$\mu_{FeCO_3}(X_{FeCO_3}(1)) = \mu_{FeCO_3}(X_{FeCO_3}(2)) \quad (7)$$

$$\mu_{CaCO_3}(X_{FeCO_3}(1)) = \mu_{CaCO_3}(X_{FeCO_3}(2)) \quad (8)$$

where the chemical potential of a non-ideal solid component in a mixture is defined as (M = Ca, Fe):

$$\mu_{MCO_3} = G_{MCO_3} + RT \ln a_{MCO_3} \quad (9)$$

Considering that, for a non-ideal solid component, the activity is the product of the activity coefficient (γ) and the mole fraction (X), eqn (9) can be rewritten as follow:

$$\mu_{MCO_3} = G_{MCO_3} + RT \ln \gamma_{MCO_3} + RT \ln X_{MCO_3} \quad (10)$$

The most frequently used function to calculate the activity coefficients in solid solutions as a function of solid composition, is the Redlich and Kister expansion (1948):[56]

$$\ln \gamma_{FeCO_3} = X_{CaCO_3}^2 \times [a_0 + a_1(3X_{FeCO_3} - X_{CaCO_3})] \quad (11)$$

$$\ln \gamma_{CaCO_3} = X_{FeCO_3}^2 \times [a_0 + a_1(3X_{CaCO_3} - X_{FeCO_3})] \quad (12)$$

Substituting these equations into the expressions of the chemical potentials and remembering that the miscibility gap boundaries (eqn (7) and (8)) should be verified, we calculate the Guggenheim parameters (a_0 and a_1) by finding the two roots of the system constituted by eqn (7) and (8). Following this procedure, we obtain $a_0 = 3.461$ and $a_1 = -0.551$, at 25 °C.

The partition of ions is commonly expressed in terms of the distribution coefficient ($D_{\{Fe/Ca\}}$) and considering the aqueous activities, $\{M^{2+}\}$:

$$D_{\left\{\frac{Fe}{Ca}\right\}} = \frac{X_{FeCO_3}}{X_{CaCO_3}} \bigg/ \frac{\{Fe^{2+}\}}{\{Ca^{2+}\}} \quad (13)$$

At equilibrium, the distribution coefficient is a function of the ratio between the solubility products of the end-members and, for non-ideal systems, it is also a function of the ratio between activity coefficients:

$$D_{\left\{\frac{Fe}{Ca}\right\},eq} = \frac{K_{CaCO_3} \times \gamma_{CaCO_3}}{K_{FeCO_3} \times \gamma_{FeCO_3}} \quad (14)$$

Solubility products and activity coefficients allow the plotting of the equilibrium distribution coefficient ($2.8 \leq D_{\{FeCa\},eq} \leq 2877$) as a function of the solid composition (Fig. 7a). A useful description of the system is obtained with a Roozeboom diagram (Fig. 7b) where the aqueous activity fraction of Fe^{2+} ($X_{Fe,aq}$) is plotted against the mole fraction of $FeCO_3$ in the solid solution.

The Roozeboom curve clearly shows that an aqueous solution supersaturated with respect to $(Ca,Fe)CO_3$ evolves
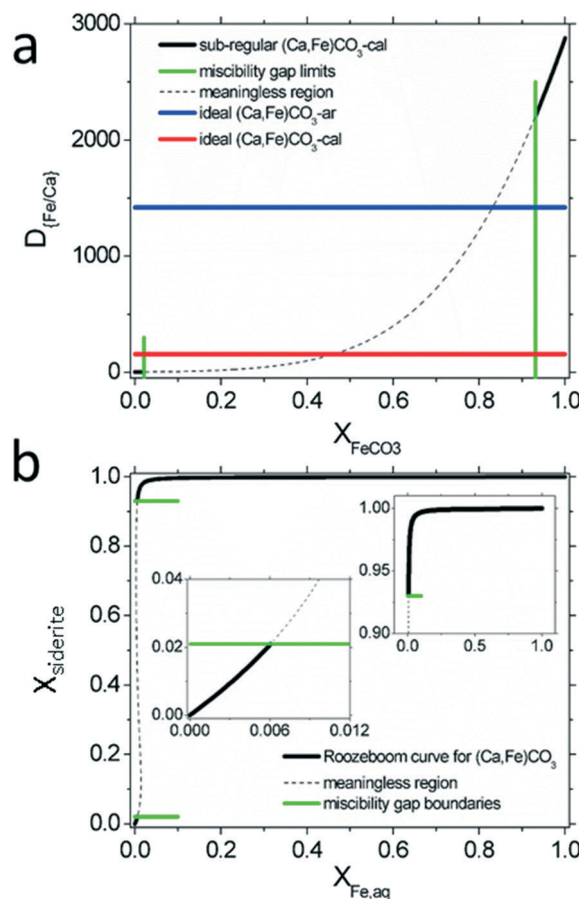

Fig. 7 a) Equilibrium distribution coefficient *versus* solid composition (in this case the *x*-axis is labelled X_{FeCO_3} to describe the mole fraction of $FeCO_3$ in both orthorhombic and rhombohedral solid solutions). b) Roozeboom diagram for calcite-siderite solid solution.

towards the equilibrium by precipitating an iron-rich solid and hence resulting in a larger {Ca}/{Fe} ratio in the aqueous phase. This behaviour was experimentally confirmed by ICP-MS measurement. Growth and nucleation experiments always revealed a strong increase in the Ca/Fe ratios after precipitation occurred. Unfortunately, in Fe-bearing systems, the formation of secondary phases makes it difficult to obtain quantitative information.

Moreover, previous work[51,57] has shown that the determination of equilibrium distribution coefficients from the compositions of liquid and solid phases during precipitation experiments is difficult because the initial supersaturation leads to "effective" distribution coefficients of ions rather than equilibrium values (*i.e.* the Roozeboom curve appears to be closer to the stoichiometric distribution value, a straight line coincident with the diagonal, as a consequence of a higher initial supersaturation). The effective ion distribution coefficients are a function of the initial supersaturation, due to kinetic and statistical reasons.[57]

The considerations above only refer to the solid solution between the end members, calcite and siderite. Both minerals occur naturally and like many carbonates they have a rhombohedral unit cell and are isostructural. To our knowledge, no analogues, natural or synthetic, for the polymorphs of $CaCO_3$ aragonite and vaterite have been reported for $FeCO_3$.

Modelling the incorporation of iron into aragonite requires estimating the free energy of formation of a hypothetical $FeCO_3$ with the aragonite-type structure. For this purpose, a powerful tool is the linear free energy relationship for crystalline solids and aqueous ions derived by Sverjensky and Molling (1992).[58] This relationship correlates the standard Gibbs free energy of formation of an isostructural family of crystalline solids with those of aqueous cations with the same charge. From their calculations, the estimated standard Gibbs free energy of formation for $FeCO_3$ with the aragonite structure is

$$\Delta G^\circ_{f,FeCO_3\text{-ar}}$$

and the corresponding solubility product is $pK_{FeCO_3\text{-ar}} = 11.27$. The distribution coefficient of an ideal solid solution between aragonite and $FeCO_3$ with the aragonite structure is:

$$D_{\left\{\frac{Fe}{Ca}\right\},ar,id} = \frac{K_{CaCO_3\text{-ar}}}{K_{FeCO_3\text{-ar}}} = 1420.2 \qquad (15)$$

Similarly, the ideal distribution coefficient between the rhombohedral phases, $D_{\{Fe/Ca\}cal,id}$, gives a value of 156.7. We observed that the orthorhombic system shows an enhanced preferential partitioning due to lower solubility of $FeCO_3\text{-ar}$ compared with siderite. The possibility to describe the non-ideality of the aragonite type $(Ca,Fe)CO_3$, under the hypothesis of a miscibility gap analogous to the rhombohedral phase, does not seem feasible due to the high iron content that we detected in the precipitated aragonite crystals (Fig. 2).

Conclusions

The data presented in this work describes the effects of Fe^{2+} on $CaCO_3$ nucleation and growth. Firstly, our experiments revealed the role played by ferrous iron on the polymorphic selection in the $CaCO_3$ system. Aragonite stabilisation induced by Fe^{2+} incorporation has important potential consequences for geological carbon storage in basalt, given that basaltic rocks have a high iron content. Magnesium is another cation that, despite its small atomic radius, tends to favour the precipitation of aragonite. Although calcite is the thermodynamically stable phase, the interaction between basalt and CO_2 dissolved in water would potentially lead to the formation of orthorhombic minerals. This has to be considered when developing geological carbon storage approaches because it is generally assumed that thermodynamic stable phases will be generated by *in situ* reactions converting basaltic rocks into carbonates.

The amount of ferrous iron was shown to play a key role in determining the induction time and the maximum free calcium, $[Ca^{2+}]$, measured during each nucleation experiment. For the Ca_T/Fe_T ratios used in this work, the presence of iron does not significantly affect ion pairing and/or any clustering phenomena in the $Ca–CO_2–H_2O$ system. Our experiments also suggest that the transient stabilisation of aqueous species, according to the dramatic increase in $[Ca^{2+}]_{max}$ before nucleation was able to occur, even under the same conditions of clustering and ion-pairing, is higher when Fe^{2+} was present. According to the direct relation between $[Ca^{2+}]_{max}$ and the actual supersaturation and assuming that the formation mechanism of $CaCO_3$, also in the presence of Fe^{2+} follows the non-classical pathway,[9,10,12] then cluster formation responds to a stabilisation needed by the aqueous medium in the presence of high ionic concentrations. By increasing the amount of Fe_{TOT} present in the system, possible $CaCO_3$ clusters, formed during the pre-nucleation stage, did not produce a nucleation event under the same conditions of supersaturation able to induce the nucleation in the absence of Fe^{2+}, and a higher supersaturation value was required in the presence of Fe^{2+}. Under these conditions, the unstable intermediates initially produced, probably amorphous,[59] could have evolved preferentially *via* the orthorhombic ordering of aragonite instead of the typical rhombohedral structure of calcite.

Growth experiments, both at the macroscopic scale and the nanoscale, clarified and quantified the inhibitory effect induced by ferrous iron on calcite growth. *In situ* AFM observations revealed that the mechanism for such inhibition can be explained by the step pinning model[41] resulting in a shortening of the average step length and subsequent distortion of normal spiral growth. This hypothesis agrees with previous work on ion incorporation into calcite.[11,42]

Using Transmission Electron Microscopy techniques we were able to measure a strong distortion of the lattice parameters in the outer layers of calcite crystals re-grown in Fe^{II}-bearing aqueous solutions. This confirms predictions made

by molecular dynamic simulations[45] and the impurity incorporation model.[10] When a few atomic layers grow preferentially incorporating foreign ions, because it is a more exothermic reaction, this preferential incorporation leads to a strained lattice where calcium ions no longer fit. Overall, our results have important implications for ankerite and ferrandolomite formation problems, because they reveal the inhibiting effects associated with the different stages of $CaCO_3$ nucleation and growth in the presence of ferrous iron.

Finally the partition coefficients for the system Ca–Fe–H_2O–CO_2 were calculated. The solid solution between calcite and siderite, $(Ca,Fe)CO_{3,rhomboedral}$, was analysed with the assumption of a sub-regular model ($a_0 = 3.46$, $a_1 = -0.55$). According to the large solubility differences between the end members ($K_{cal}/K_{sid} = 156.7$), the distribution coefficient calculated as a function of solid composition results in values between 2.8 and 3.5 for Ca-rich solids outside the miscibility gap ($X_{Fe} \leq 0.02$). Using the linear free energy equation for aqueous ions and crystalline solids,[58] it was possible to estimate the ideal distribution coefficient for the solid solution $(Ca,Fe)CO_{3,orthorhombic}$. A comparison between the calculated value for aragonite-type and calcite-type $(Ca,Fe)CO_3$ lattices shows how the ideal distribution coefficient was about one order of magnitude larger in the orthorhombic solid solution than in the rhombohedral one. According to this model, the amount of iron in precipitated aragonite crystals should be larger than in calcite, and this has been confirmed experimentally in this work.

Acknowledgements

References

1 E. H. Oelkers and D. R. Cole, Carbon dioxide sequestration: A solution to global problem, *Elements*, 2008, **4**(5), 305–310.

2 E. S. Rubin, CO2 Capture and Transport, *Elements*, 2008, **4**(5), 311–317.

3 D. R. Cole and E. H. Oelkers, Carbon Dioxide Sequestration, *Elements*, 2008, **4**(5), 287–362.

4 D. J. DePaolo, D. R. Cole, A. Navrotsky and I. C. Bourg, Geochemistry of Geologic CO_2 Sequestration, *Rev. Mineral. Geochem.*, 2013, **77**, 1–539.

5 L. Marini, *Geological Sequestration of Carbon Dioxide: Thermodynamics, Kinetics and reaction path modelling*, Elsevier Science, Amsterdam, 1st edn, 2006.

6 S. R. Gislason and E. H. Oelkers, Carbon Storage in Basalt, *Science*, 2014, **344**, 373–374.

7 J. M. Matter, W. S. Broecker, S. R. Gislason, E. Gunnlaugsson, E. H. Oelkers, M. Stute, H. Sigurdardóttir, A. Stefansson, H. A. Alfreðsson, E. S. Aradóttir, G. Axelsson, B. Sigfússon and D. Wolff-Boenisch, The CarbFix Pilot Project – Storing Carbon Dioxide in Basalt, *Energy Procedia*, 2011, **4**, 5579–5585.

8 A. V. Radha and A. Navrotsky, Thermodynamics of Carbonates, *Rev. Mineral. Geochem.*, 2013, **77**, 73–121, DOI: 10.2138/rmg.2013.77.3.

9 D. Gebauer, A. Völkel and H. Cölfen, Stable pre-nucleation calcium carbonate clusters, *Science*, 2008, **322**, 1819–1822, DOI: 10.1126/science.1164271.

10 J. J. De Yoreo, L. A. Zepeda-Ruiz, R. W. Friddle, S. R. Qiu, L. E. Wasylenki, A. A. Chernov and P. M. Dove, Rethinking Classical Crystal Growth Models through Molecular Scale Insights: Consequences of Kink-Limited Kinetics, *Cryst. Growth Des.*, 2009, **9**(12), 5135–5144, DOI: 10.1021/cg900543g.

11 E. Ruiz-Agudo, C. V. Putnis, L. J. Wang and A. Putnis, Specific effects of background electrolytes on the kinetics of step propagation during calcite growth, *Geochim. Cosmochim. Acta*, 2011, **75**, 3803–3814.

12 C. Rodriguez-Navarro, K. Kudłacz, Ö. Cizer and E. Ruiz-Agudo, Formation of Amorphous Calcium Carbonate and its Transformation into Mesostructured Calcite, *CrystEngComm*, 2015, **17**, 58–72.

13 J. D. Rodriguez-Blanco, S. Shaw and L. G. Benning, The kinetics and mechanisms of amorphous calcium carbonate (ACC) crystallization to calcite, via vaterite, *Nanoscale*, 2011, **3**, 265–271.

14 M. Prieto, P. Cubillas and A. Fernández-Gonzalez, Uptake of dissolved Cd by biogenetic and abiogenic aragonite: a comparison with sorption onto calcite, *Geochim. Cosmochim. Acta*, 2003, **67**, 3859–3869.

15 M. E. Berndt and W. E. Seyfried, Rates of aragonite conversion to calcite in dilute aqueous fluids at 50 to 100 °C: Experimental calibration using Ca-isotope attenuation, *Geochim. Cosmochim. Acta*, 1999, **63**, 373–381.

16 P. E. Rosenberg, Subsolidus relations in the system $CaCO_3$-$FeCO_3$, *Am. J. Sci.*, 1963, **261**, 683–690.

17 P. E. Rosenberg, Subsolidus relations in the system $CaCO_3$-$MgCO_3$-$FeCO_3$ between 350 and 550 °C, *Am. Mineral.*, 1967, **52**, 787–796.

18 J. R. Goldsmith, D. L. Graf, J. Witters and D. A. Northrop, Studies in the system $CaCO_3$-$MgCO_3$-$FeCO_3$: 1. Phase relations; 2. A method for major-element spectrochemical analysis; 3. Compositions of some ferroan dolomites, *J. Geol.*, 1962, **70**, 659–688.

19 L. Chai and A. Navrotsky, Synthesis, characterization, and energetics of solid solution along the dolomite-ankerite join, and implications for the stability of ordered CaFe(CO3)₂, *Am. Mineral.*, 1996, **81**, 1141–1147.

20 P. L. Fosbøl, K. Thomsen and E. H. Stenby, Review and recommended thermodynamic properties of $FeCO_3$, *Corros. Eng., Sci. Technol.*, 2010, **45**(2), 115–135.

21 P. A. van Aken, V. J. Styrsa and B. Liebscher, Quantitative determination of iron oxidation states in minerals using Fe $L_{2,3}$-edge electron energy-loss near-edge structure spectroscopy, *Phys. Chem. Miner.*, 1998, **25**(5), 323–327.

22 M. B. Tomson and G. H. Nancollas, Mineralisation Kinetics; A Constant Composition Approach, *Science*, 1978, **200**, 1059–1060.

23 R. Beck, M. Seiersten and J. P. Andreassen, The constant composition method for crystallization of calcium carbonate at constant supersaturation, *J. Cryst. Growth*, 2013, **380**, 187–196, DOI: 10.1016/j.jcrysgro.2013.05.038.

24 J. L. Katz, M. R. Reick, R. E. Herzog and K. I. Parsiegla, Calcite Growth Inhibition by Iron, *Langmuir*, 1993, **9**, 1423–1430.

25 C. W. Davies and A. L. Jones, The precipitation of Silver Chloride from Aqueous Solutions. Part 2. Kinetics of growth of Seed Crystals, *Trans. Faraday Soc.*, 1955, **51**, 812–817.

26 J. Zhang and G. H. Nancollas, Mechanisms of Growth and Dissolution of Sparingly Soluble Salts, *Rev. Mineral. Geochem.*, 1990, **23**, 365–396.

27 I. B. Butler, M. A. Schoonen and D. T. Rickard, Removal of dissolved oxygen from water: A comparison of four common techniques, *Talanta*, 1994, **41**, 211–215.

28 W. Stumm and G. F. Lee, Oxygenation of Ferrous Iron, *Indian Chem. Eng.*, 1961, **53**, 143–146.

29 D. L. Parkhurst and C. A. J. Appelo, *Description of input and examples for Phreeqc version 3. A computer program for speciation, batch-reaction, one-dimensional transport, and inverse geochemical calculations*, U.S. Geological Survey, Denver, 2013, http://pubs.usgs.gov/tm/06/a43.

30 Y. P. Lin and P. C. Singer, Effect of Mg^{2+} on the kinetics of calcite crystal growth, *J. Cryst. Growth*, 2009, **312**, 136–140, DOI: 10.1016/j.jcrysgro.2009.09.041.

31 E. Ruiz-Agudo and C. V. Putnis, Direct observations of mineral-fluid reactions using atomic force microscopy: the specific example of calcite, *Mineral. Mag.*, 2012, **76**, 227–253.

32 R. J. Reeder, Crystal Chemistry of the Rhombohedral Carbonates, *Rev. Mineral. Geochem.*, 1983, **11**, 1–48.

33 H. H. Teng, P. M. Dove and J. J. De Yoreo, Kinetics of calcite growth: Surface processes and relationships to macroscopic rate laws, *Geochim. Cosmochim. Acta*, 2000, **64**, 2255–2266.

34 K. Larsen, K. Bechgaard and S. L. S. Stipp, The effect of the Ca^{2+} to CO_3^{2-} activity ratio on spiral growth at the calcite {10$\bar{1}$4} surface, *Geochim. Cosmochim. Acta*, 2010, **74**(7), 2099–2109, DOI: 10.1016/j.gca.2009.12.028.

35 A. Hamdouni, G. Montes-Hernandez, M. Tlili, N. Findling, F. Renard and C. V. Putnis, Removal of Fe(II) from groundwater via aqueous portlandite carbonation and calcite-solution interactions, *Chem. Eng. J.*, 2016, **283**, 404–411, DOI: 10.1016/j.cej.2015.07.077.

36 E. L. Dromgoole and L. M. Walter, Iron and manganese incorporation into calcite: Effects of growth kinetics, temperature and solution chemistry, *Chem. Geol.*, 1990, **81**, 311–336.

37 N. Wada, K. Yamashita and T. Umegaki, Effects of divalent cations upon nucleation, growth and transformation of calcium carbonate polymorphs under conditions of double diffusion, *J. Cryst. Growth*, 1995, **148**, 297–304, DOI: 10.1016/0022-0248(94)00880-9.

38 E. Loste, R. M. Wilson, R. Seshadri and F. C. Meldrum, The role of magnesium in stabilising amorphous calcium carbonate and controlling calcite morphologies, *J. Cryst. Growth*, 2003, **254**, 206–218.

39 L. Fernández-Díaz, J. M. Astilleros and C. M. Pina, The morphology of calcite crystals grown in a porous medium doped with divalent cations, *Chem. Geol.*, 2006, **225**, 314–321.

40 J. González-López, S. E. Ruiz-Hernández, A. Fernández-González, A. Jiménez, N. H. de Leeuw and R. Grau-Crespo, Cobalt incorporation in calcite: Thermochemistry of (Ca,Co)CO_3 solid solutions from density functional theory simulations, *Geochim. Cosmochim. Acta*, 2014, **142**, 205–216.

41 N. Cabrera and D. A. Vermilyea, The Growth of Crystals from Solution, in: *Growth and Perfection of Crystals*, Proceedings of an International Conference on Crystal Growth held at Cooperstown, Wiley, New York, 1958.

42 J. J. De Yoreo and P. G. Vekilov, Principles of Crystal Nucleation and Growth, *Rev. Mineral. Geochem.*, 2003, **54**, 57–94.

43 J. W. Mullin, *Crystallization*, Butterworth Heineman, Oxford, 4th edn, 2001.

44 J. M. Astilleros, L. Fernández-Díaz and A. Putnis, The role of magnesium in the growth of calcite: An AFM study, *Chem. Geol.*, 2010, **271**, 52–58.

45 N. H. De Leeuw, Molecular Dynamics Simulations of the Growth Inhibiting Effect of Fe^{2+}, Mg^{2+}, Cd^{2+} and Sr^{2+} on Calcite Crystal Growth, *J. Phys. Chem. B*, 2002, **106**, 5241–5249.

46 R. D. Shannon, Revised effective ionic radii and systematic studies of interatomic distances in halides and chalcogenides, *Acta Crystallogr., Sect. A: Cryst. Phys., Diffr., Theor. Gen. Crystallogr.*, 1976, **32**, 751–767.

47 P. Raiteri, R. Demichelis and J. D. Gale, Thermodynamically Consistent Force Field for Molecular Dynamics Simulations of Alkaline-Earth Carbonates and Their Aqueous Speciation, *J. Phys. Chem. C*, 2015, **119**, 24447–24458.

48 J. M. Zachara, C. E. Cowan and C. T. Resch, Sorption of divalent metals on calcite, *Geochim. Cosmochim. Acta*, 1991, **55**, 1549–1562.

49 P. M. Davidson, Ternary iron, magnesium, calcium carbonates: A thermodynamic model for dolomite as an ordered derivative of calcite-structure solutions, *Am. Mineral.*, 1994, **79**, 332–339.

50 E. A. Guggenheim, Theoretical basis of Raoult's law, *Trans. Faraday Soc.*, 1937, **33**, 151–156.

51 M. Prieto, Thermodynamics of ion partitioning in solid solution – aqueous solution systems, *EMU Notes Mineral.*, 2010, vol. 10, pp. 1–42.

52 P. D. Glynn, Solid-Solution Solubilities and Thermodynamics: Sulfates, Carbonates and Halides, *Rev. Mineral. Geochem.*, 2000, **40**, 481–512.

53 P. D. Glynn and E. J. Reardon, Solid-solution aqueous-solution equilibria: thermodynamic theory and representation, *Am. J. Sci.*, 1990, **278**, 164–201.

54 P. D. Glynn, E. J. Reardon, L. N. Plummer and E. Busenberg, Reaction paths and equilibrium end-points in solid-solution aqueous-solution systems, *Geochim. Cosmochim. Acta*, 1990, **54**, 267–282.

55 M. Prieto, Thermodynamics of solid solution-aqueous solution systems, *Rev. Mineral. Geochem.*, 2009, **70**, 47–85.

56 O. Redlich and A. T. Kister, Algebraic representation of the thermodynamic properties and the classification of solutions, *Ind. Eng. Chem.*, 1948, **40**, 345–348.

57 A. Putnis, Effects of kinetics and mechanisms of crystal growth on ion-partitioning in solid solution-aqueous solution (SS-AS) systems, *EMU Notes Mineral.*, 2010, vol. 10, pp. 43–64.

58 D. A. Sverjensky and P. A. Molling, A linear free energy relationship for crystalline solids and aqueous ions, *Nature*, 1992, **356**, 231–234.

59 O. Sel, A. V. Radha, K. Dideriksen and A. Navrotsky, Amorphous iron(II) carbonate: Crystallization energetics and comparison to other carbonate minerals related to CO_2 sequestration, *Geochim. Cosmochim. Acta*, 2012, **87**, 61–88.